

Stable Formamidinium-Based Perovskite Solar Cells via In Situ Grain Encapsulation

Tanghao Liu, Yuanyuan Zhou,* Zhen Li, Lin Zhang, Ming-Gang Ju, Deying Luo, Ye Yang, Mengjin Yang, Dong Hoe Kim, Wenqiang Yang, Nitin P. Padture, Matthew C. Beard, Xiao Cheng Zeng, Kai Zhu,* Qihuang Gong, and Rui Zhu*

Formamidinium (FA)-based lead iodide perovskites have emerged as the most promising light-absorber materials in the prevailing perovskite solar cells (PSCs). However, they suffer from the phase-instability issue in the ambient atmosphere, which is holding back the realization of the full potential of FA-based PSCs in the context of high efficiency and stability. Herein, the tetraethylorthosilicate hydrolysis process is integrated with the solution crystallization of FA-based perovskites, forming a new film structure with individual perovskite grains encapsulated by amorphous silica layers that are in situ formed at the nanoscale. The silica not only protects perovskite grains from the degradation but also enhances the charge-carrier dynamics of perovskite films. The underlying mechanism is discussed using a joint experiment-theory approach. Through this in situ grain encapsulation method, PSCs show an efficiency close to 20% with an impressive 97% retention after 1000-h storage under ambient conditions.

Owing to the low material cost and excellent optoelectronic properties, organic–inorganic halide perovskites have been introduced as a new family of light absorber materials that are catalyzing a revolution in the field of photovoltaics (PVs).^[1–3] Since the first use of organic–inorganic halide perovskite in solar cells by Kojima et al.,^[4] the power conversion efficiency (PCE) of perovskite-based solar cells (PSCs) has reached a

certified value of 22.7%.^[5–17] While methylammonium lead iodide (MAPbI₃) was the most widely studied perovskite in the early development of PSCs, the light-harvesting capability of MAPbI₃ in the infrared-red region of the solar spectrum is limited by its relatively large bandgap (≈ 1.55 eV).^[18] It also suffers from low intrinsic/thermal stability due to the volatile MA⁺ component. In this context, substantial effort has been now focused on formamidinium lead iodide (FAPbI₃) perovskite which exhibits a more ideal bandgap (≈ 1.48 eV) and significantly enhanced thermal stability.^[19,20] In spite of these clear advantages, under ambient conditions, FAPbI₃ favors a non-perovskite polymorph (δ -FAPbI₃, hexagonal) instead of the useful perovskite polymorph (α -FAPbI₃, cubic),^[20,21] which is the major hurdle that is holding back the realization of the full potential of FAPbI₃-based PSCs in the context of high efficiency and stability.^[22,23] In order to mitigate this issue, vast research activities have been performed, which mainly focus on the composition engineering of FAPbI₃ perovskite. It has been shown that incorporation of monovalent cations, such as cesium (Cs⁺),^[24,25] rubidium (Rb⁺),^[26] butylammonium,^[27] and phenylethylammonium,^[28,29] either into the

T. Liu, D. Luo, W. Yang, Prof. Q. Gong, Prof. R. Zhu
State Key Laboratory for Artificial Microstructure
and Mesoscopic Physics
Department of Physics
Peking University
Beijing 100871, China
E-mail: iamzhurui@pku.edu.cn

Prof. Y. Zhou, Dr. L. Zhang, Prof. N. P. Padture
School of Engineering
Brown University
Providence, RI 02912, USA
E-mail: yuanyuan_zhou@brown.edu

Dr. Z. Li, Dr. Y. Yang, Dr. M. Yang, Dr. D. H. Kim, Dr. M. C. Beard, Dr. K. Zhu
Chemistry and Nanoscience Center
National Renewable Energy Laboratory
Golden, CO 80401, USA
E-mail: Kai.Zhu@nrel.gov

Dr. Z. Li
Center for Nano Energy Materials
Northwestern Polytechnical University
Xi'an 710072, China

Dr. M.-G. Ju, Prof. X. C. Zeng
Department of Chemistry
University of Nebraska-Lincoln
Lincoln, NE 68588, USA

Prof. Q. Gong, Prof. R. Zhu
Collaborative Innovation Center of Quantum Matter
Beijing 100871, China

Prof. Q. Gong, Prof. R. Zhu
Collaborative Innovation Center of Extreme Optics
Shanxi University
Taiyuan, Shanxi 030006, China

 The ORCID identification number(s) for the author(s) of this article can be found under <https://doi.org/10.1002/aenm.201800232>.

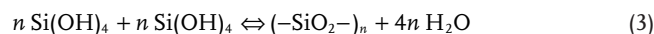
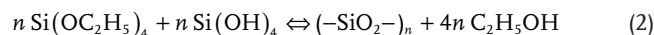
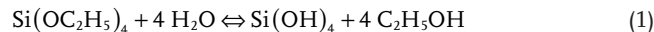
DOI: 10.1002/aenm.201800232

FAPbI₃ crystal lattice or crystal surface, obviously stabilizes the perovskite polymorph of FAPbI₃ and enhances the PCE and stability of PSC devices. However, regardless of these impressive improvements, these composition-engineered FA-based perovskite films are still sensitive to the ambient conditions and far from satisfactory for real-world applications.^[3]

To further boost the stability of FA-based perovskite films, herein a new strategy is proposed, which entails encapsulation of individual perovskite grains with thin layers of amorphous silica at the nanoscale. To prepare this unique silica-perovskite nanocomposite structure, we have rationally integrated the tetraethylorthosilicate (TEOS) hydrolysis into the solution crystallization of FA-based perovskites using a simple “one-pot” solution approach, through which the silica-encapsulated perovskite grains are in situ formed. The aim of this strategy is to complement rather than replace those successful “composition-engineering” methods.^[10,14,15,24,26] In this context, one of the state-of-the-art FA-based perovskite compositions, FA_{0.85}Cs_{0.15}PbI₃, has been chosen in this study for the proof-of-concept demonstration. It is revealed that this silica encapsulation strategy prevents FA-based perovskite grains from the degradation in ambient atmosphere by retarding the perovskite-to-nonperovskite phase transformation. Furthermore, the amorphous silica layer enhances the charge-carrier dynamics in the FA-based perovskite films. And thus, FA-based PSCs exhibit high PCE approaching 20% which is impressively stable for 1000 h under ambient conditions.

It is well known that silica can be synthesized through the hydrolysis reaction of TEOS in the presence of water, which is a purely solution-based sol-gel process.^[30] It is then easy to perform this hydrolysis reaction in the FA_{0.85}Cs_{0.15}PbI₃ perovskite precursor solution by simply co-adding TEOS and water into the perovskite precursor solution as shown in **Figure 1A**.

After aging the solution for a controlled time period, a series of hydrolysis/condensation reactions occur in the solution, which convert the TEOS molecules into silica gels via Si–O–Si linkages (see **Figure 1B**). The detailed chemical reactions in this process are given below^[30,31]



After these reactions, the FA_{0.85}Cs_{0.15}PbI₃ precursor solution containing silica oligomers is ready for the spin coating-based thin-film processing. **Figure 1C** schematically illustrates the microstructure evolution of the FA_{0.85}Cs_{0.15}PbI₃ perovskite film with the presence of silica oligomers. The crystallization of FA_{0.85}Cs_{0.15}PbI₃ perovskite grains and the precipitation of silica are expected to occur simultaneously, forming a perovskite-silica composite film. The microstructure of final perovskite-silica composite film is expected to be influenced by the amount and polymerization degree of the silica oligomers in the precursor solution, since the silica serves as heterogeneous nucleation sites for the perovskite crystallization and meanwhile constrains the perovskite crystallization behavior at the nanoscale. Therefore, in this study, the hydrolysis time is fixed at 30 min and the optimal adding amount of TEOS is 3% v/v. Perovskite films prepared with this method are denoted as FAPI-T, and those without using TEOS are denoted as FAPI.

In **Figure 2A**, the top-view scanning electron microscope (SEM) image of the FAPI-T film is shown. The FAPI-T film exhibits a very compact, well-defined grain morphology, which

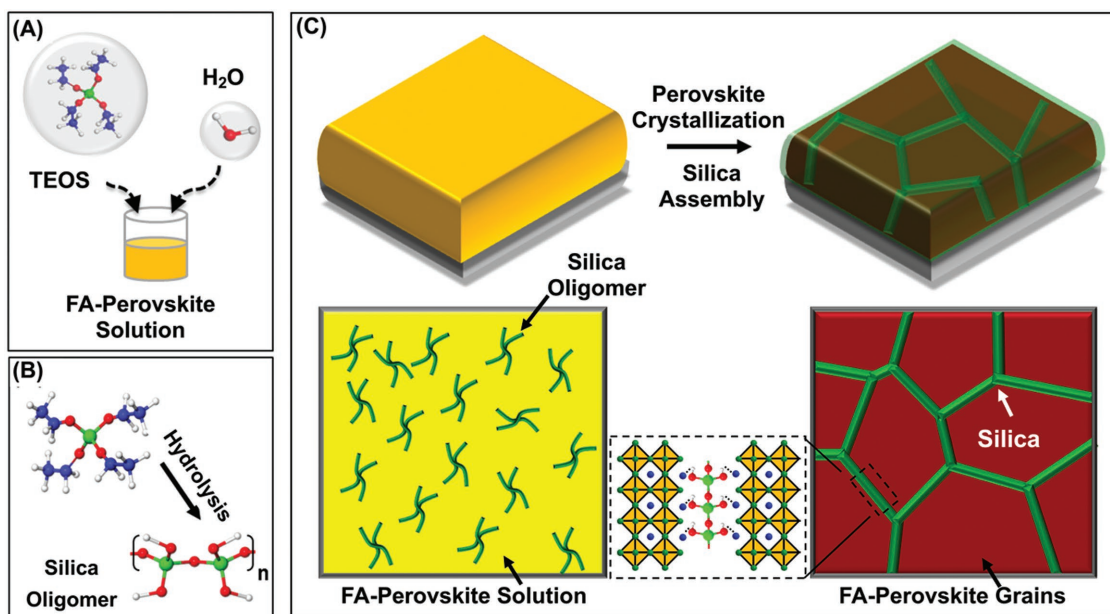


Figure 1. Schematic illustration showing A) the mixing of the FA-based perovskite precursor solution and the silica precursors in “one pot,” B) the formation of silica oligomers via the hydrolysis reaction of TEOS with water, and C) the formation process of the FA-based perovskite film consisting of individual silica-encapsulated grains from the silica-oligomers-containing precursor solution.

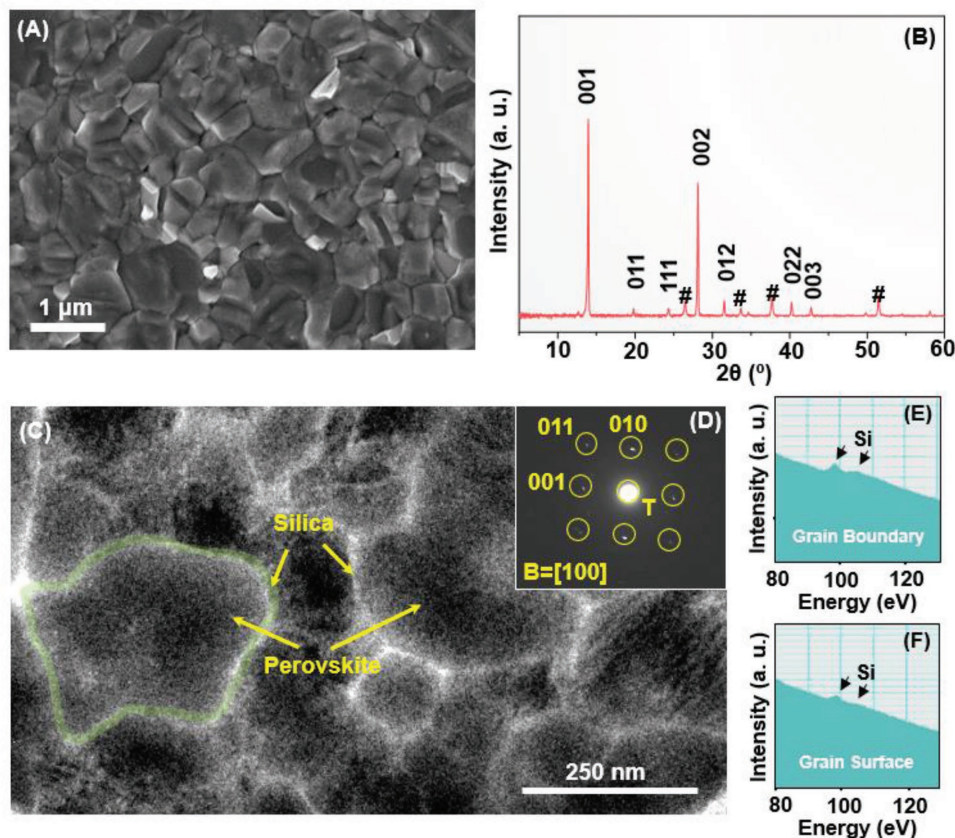


Figure 2. A) Top-view SEM image and B) XRD pattern of the silica-incorporated FA_{0.85}CS_{0.15}PbI₃ perovskite (FAPI-T) film. The XRD pattern is indexed based on the cubic symmetry (space group *Pm-3m*) of the perovskite. C) Bring-field TEM image showing FAPI-T film consists of silica-encapsulated perovskite grains. One typical amorphous silica layer marked (light contrast). D) SAEDP obtained at the center of one typical silica-encapsulated grain showing its single-crystalline nature across the film thickness. E, F) Si L-edge EELS spectra measured at the centers of the silica layer (grain boundary) and perovskite grain (grain surface).

confirms that the optimal TEOS addition does not have any detrimental effect on the film uniformity. The mean grain size in the FAPI-T film is ≈ 670 nm, which is only slightly reduced compared with that in the reference FAPI film (Figure S1, Supporting Information). No obvious agglomeration of silica can be observed, confirming the highly uniform dispersion of the silica within the film. Figure 2B shows the X-ray diffraction (XRD) pattern of the FAPI-T film. All the observed diffraction peaks can be assigned to the FA_{0.85}CS_{0.15}PbI₃ perovskite phase, confirming the high phase-purity and crystallinity of the perovskite phase in the film. No diffraction peak is observed for the incorporated silica in the film, which reveals again that the silica derived from the TEOS hydrolysis process is amorphous.^[31] When the adding amount of TEOS increases to 10% v/v, an obvious reduction in grain size is observed in the film (FAPI-10T) in Figure S1 in the Supporting Information, which is usually unfavorable for charge transport. Furthermore, the crystallinity of FAPI-T film gradually decreases with the increase of hydrolysis time as reflected by XRD results in Figure S2 in the Supporting Information. This is most probably due to the fact that longer hydrolysis time will lead to a higher polymerization degree of silica which constrains the perovskite growth more significantly. As seen in Figure S3 in the Supporting Information, when the hydrolysis time is longer than 120 h, the precursor solution becomes completely

gel-like and lose flowability. These results highlight the importance of controlling the hydrolysis conditions for achieving desirable film structures. And it is imperative that the desirable microstructural features (large grain, high crystallinity, uniform, phase pure) of the pristine perovskite film can be retained after the silica incorporation.

Transmission electron microscopy (TEM) characterization is then performed to unravel the detailed microstructure in the FAPI-T film. The TEM sample is prepared by directly depositing the FAPI-T film on the TEM grid. Such sample preparation method can avoid any possible damage in the “soft” perovskites, which has been confirmed previously by us and others.^[32,33] Especially, we have observed that FAPbI₃-based perovskite materials are very sensitive to the high-energy-density ion beams. Hence, the focus-ion-beam-based TEM-sample preparation technique is avoided here.^[32,33] Figure 2C is the bright-field TEM image of the FAPI-T film. From the image contrast, the perovskite grain (dark-contrast) and silica-consisting grain boundary (light-contrast) regions are immediately differentiated. A higher magnification TEM image is shown in Figure S4 in the Supporting Information, which displays the amorphous silica and crystalline perovskite grains more clearly. The thickness of the amorphous silica layer is around 6 nm. We emphasize that the grain boundary

structure with amorphous silica secondary-phase is clearly different from the typical grain boundary structure with well-defined misorientation in those phase-pure perovskite materials.^[34] In Figure 2D, the selected-area electron-diffraction pattern (SAEDP) is obtained for a typical silica-encapsulated grain, which confirms the single-crystalline nature of the grain across the film thickness. The SAEDP pattern is indexed and fully consistent with the cubic structure of FA_{0.85}CS_{0.15}PbI₃ perovskite. This also suggests that the silica component is not incorporated into perovskite crystal structure. To confirm the location of the incorporated silica, electron-energy loss spectra (EELS) were recorded from the Si L-edge at centers of the amorphous grain boundary (Figure 2E) and the crystalline perovskite grain (Figure 2F). Both spectra show the signal of Si element. In addition, the EELS peak intensity of Si is found to be relatively higher in the grain boundary region. It indicates that there is more silica in the grain boundary than on the grain

surface, which is very consistent with the expected nanocomposite geometry schematically shown in Figure 1C. Although the “softness” of the FA-based perovskite materials precludes performing more detailed elemental analyses, all these characterization results have provided solid evidence that the silica-encapsulated grain structure forms successfully in the FAPI-T film.

Transient absorption (TA) spectroscopy studies are then performed to reveal the charge-carrier dynamics in the FAPI-T and FAPI films. The exciton bleach tracks the presence and decay of free charge carriers. The major decay of carriers arises from recombination at top and bottom surfaces and from recombination within the interior of the films.^[35,36] With this assumption, the surface recombination velocity (S) and bulk lifetime (τ_B) can be extracted from the following approximate equation, $1/\tau_{TA} = 2S/L + 1/\tau_B$, where τ_{TA} is the total carrier lifetime and L is the film thickness. Figure 3A,B shows the

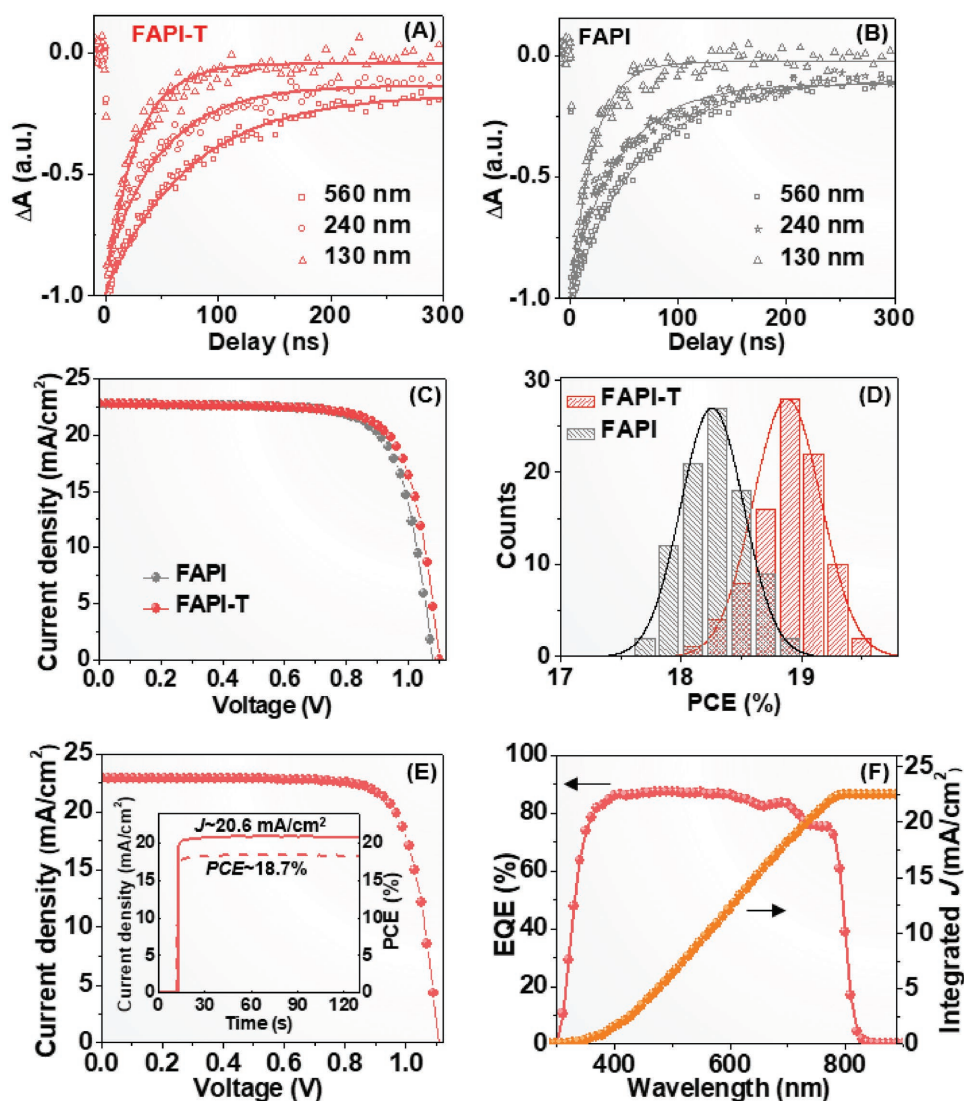


Figure 3. TA spectra of A) FAPI-T and B) FAPI films with various thicknesses (560, 240, and 130 nm). C) Typical J - V curves and D) PCE histograms of PSCs made using FAPI-T and FAPI films. E) J - V curve and F) EQE spectrum of the champion PSC made using the FAPI-T film. Inset in (E) is the stabilized outputs of J and PCE at the maximum-power-point voltage ($V = 0.91$ V).

exciton bleach recovery dynamics obtained from TA measurements for the FAPI-T and FAPI film samples with various thicknesses (560, 240, and 130 nm), respectively. The measured carrier-dynamics can be described using single-exponential equation, $A_0(t) = A_0 \cdot \exp(-t/\tau_{TA})$, with an offset. Plotting the total carrier lifetime as function of film thickness allows for separating the contribution from surface recombination and bulk recombination. The results show similar bulk recombination lifetimes ($\tau_B \approx 167$ ns) but different surface recombination velocities for the two films. The S values of the FAPI and FAPI-T films are determined to be 243 and 160 cm^{-1} , respectively, which indicate significantly reduced defects/traps on the film surface. The beneficial effect of silica on carrier dynamics is also supported by the stronger steady-state photoluminescence (PL) emission in FAPI-T film (Figure S5, Supporting Information). In this context, it is concluded that the optimal silica incorporation does not have a negative impact on the charge dynamics in the film bulk including grain boundaries. Meanwhile, it leads to effective passivation on film surfaces. As a result, the overall charge-carrier dynamics of the film is improved by the silica layer. These findings are also consistent with the previous finding that the film surface properties are more prominent in determining the carrier dynamics in polycrystalline halide perovskite films.^[35,37] It is important to emphasize that, although no obvious improvement in charge-carrier dynamics is contributed by the silica at grain boundaries in this study, such portion of silica is indispensable for enhancing the film stability, which is discussed later.

Planar-heterojunction PSCs were then fabricated to evaluate the photovoltaic performance of the FAPI and FAPI-T films. Typical Spiro-OMeTAD/Au cathodes and TiO₂/fluorinated tin oxide (FTO) anodes are used in these PSCs. A typical cross-sectional SEM image of the PSC is shown in Figure S6 in the Supporting Information, where each PSC layer is labeled. Typical current density–voltage (J – V) curves are plotted in Figure 3C, and the extracted photovoltaic parameters are summarized in Table S1 in the Supporting Information. The PSC made using the silica-free FAPI film delivers PCE of 18.2% with short-circuit current density (J_{sc}) of 22.8 mA cm^{-2} , open-circuit voltage (V_{oc}) of 1.08 V, and fill factor (FF) of 0.74. With the addition of TEOS, the overall PCE is boosted to 18.8% in the FAPI-T film-based PSC. The photovoltaic parameter that is most obviously improved is V_{oc} (from 1.08 to 1.10 V), which is consistent with the reduction of defects/traps and the suppression of nonradiative recombination in the FAPI-T film as revealed by the TA results (Figure 3A,B). PSC devices are also fabricated with more TEOS addition (10% v/v) in the precursor solution, which deliver much poorer performance (see Figure S7 and Table S1, Supporting Information). This can be attributed to the insulating nature of thick silica layers which can negatively affect the charge transport. This again reflects the importance of optimizing the silica incorporation. More systematic studies on this topic is undergoing. Figure 3D compares the PCE statistics of PSCs made using FAPI-T and FAPI films, which confirms the reproducibility of the beneficial effect of the silica incorporation on the overall PSC performance. Additional experiments are also performed to exclude the possible effect of H₂O,^[11,38] which is incorporated in the precursor solution associated with TEOS addition, on the device performance. The

results show that when only H₂O is added into the precursor solution, the microstructure of the film does not show notable difference as reflected by the SEM and XRD results in Figures S8 and S9 in the Supporting Information. There is either no obvious change in the device performance (Figure S10, Supporting Information) when the PSC is processed with only H₂O addition. In Figure 3E, the J – V curve of the champion device based on FAPI-T is shown, which displays PCE of 19.5% with J_{sc} of 22.8 mA cm^{-2} , V_{oc} of 1.11 V, and FF of 0.77. The steady-state PCE output of this device (see the inset of Figure 3E) is monitored at the maximum-power-point voltage ($V = 0.91$ V). A stabilized photocurrent density (J) of 20.6 mA cm^{-2} and a stabilized PCE of 18.7% are achieved immediately upon one-sun illumination. The external quantum efficiency (EQE) spectrum of the same PSC is recorded in Figure 3F, where the integrated current density is 22.5 mA cm^{-2} , a value close to the J_{sc} extracted from the J – V curve in Figure 3E.

Regarding the stability, the ambient stability is the most concerned issue for FA-based perovskites.^[39] While these perovskites have been proven to be able to sustain high thermal/light stresses,^[18,40] their perovskite phase-stability is still low due to the presence of thermodynamically more stable nonperovskite polymorph in the ambient conditions. In this context, we have performed accelerated ambient-stability tests by storing the film samples in the climate chamber with a high constant relative humidity (RH) of 80% at 25 °C. XRD patterns of the FAPI-T and FAPI films before and after 2 h storage are compared in Figure 4A,B. For the FAPI-T film, it is seen that the intensity of the characteristic 100 peak of FA_{0.85}Cs_{0.15}PbI₃ perovskite is well maintained, and no peak associated with the degradation phases, such as δ -phase FA_{0.85}Cs_{0.15}PbI₃ nonperovskite or PbI₂, is observed. Correspondingly, in Figure 4C, there is no noticeable reduction in the absorption in the entire wavelength range of the UV–vis absorption spectra for the FAPI-T film. In contrast, for the FAPI film, a significant amount of δ -phase FA_{0.85}Cs_{0.15}PbI₃ nonperovskite has evolved after the storage under the exactly same conditions, accompanied by the reduction in the intensity of 100 peak in the XRD pattern (Figure 4B). The UV–vis absorption spectra also show a significant reduction in the light absorption above the bandgap energy of FA_{0.85}Cs_{0.15}PbI₃ perovskite (Figure 4D). All these results confirm that the silica-incorporated FAPI-T film is much more ambient-stable than the silica-free FAPI film. Note that the FA_{0.85}Cs_{0.15}PbI₃ perovskite has already shown substantially higher stability than the FAPbI₃ perovskite in our previous study,^[24] and thus, the stability of the FAPI-T film is striking. This high stability can be attributed to two beneficial effects of the unique silica-perovskite nanocomposite structure. First, it is natural that silica protects FA_{0.85}Cs_{0.15}PbI₃ grains from the ambient moisture and slows down the phase-transformation reaction of FA_{0.85}Cs_{0.15}PbI₃ from perovskite (α -phase) to nonperovskite (δ -phase). Second, we have also found that the silica encapsulation layer has an impact on the intrinsic or thermodynamic stability of the perovskite grains based on a theoretical approach. The thermodynamic stability of α and δ phases of FA_{0.85}Cs_{0.15}PbI₃ with and without the presence of the FA_{0.85}Cs_{0.15}PbI₃/silica interface are assessed using density functional theory (DFT)-based first-principle calculations. As schematically shown in Figure 4E, the energy

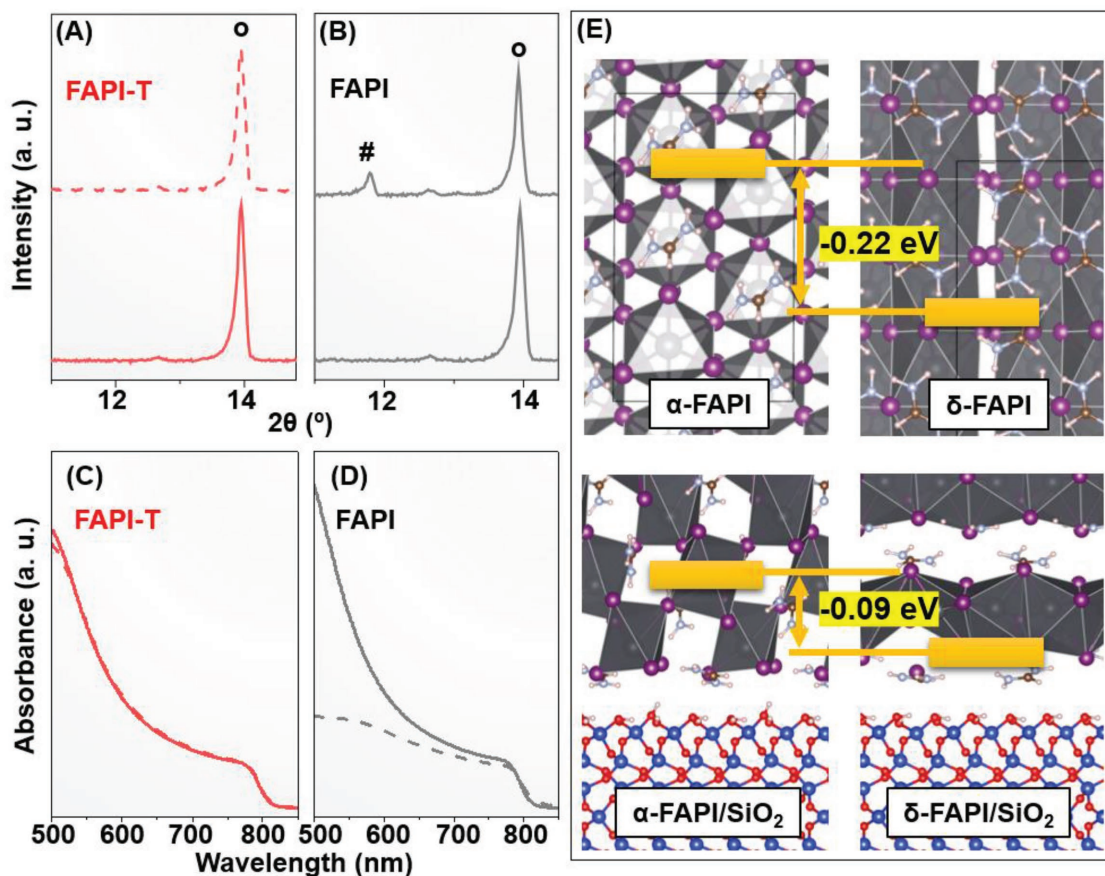


Figure 4. XRD patterns of the A) FAPI-T and B) FAPI films before (solid curve) and after (dash curve) storage in the climate chamber (25 °C, 80% RH). UV-vis spectra of the C) FAPI-T and D) FAPI films before (solid curve) and after (dash curve) storage in the climate chamber (25 °C, 80% RH). E) DFT-computed energy difference between α and δ phase FA-based perovskite with and without a silica-perovskite interface.

difference (ΔE) between the α and δ phases with the presence of the $\text{FA}_{0.85}\text{Cs}_{0.15}\text{PbI}_3/\text{silica}$ interface is 0.09 eV, which is less than half of the ΔE (0.22 eV) for the silica-free case. This indicates that the driving force for $\alpha \rightarrow \delta$ phase transformation has been significantly reduced with the introduction of silica/perovskite interfaces. Especially, the silica-perovskite nanocomposite in this study possesses an ideal structure that contains perfect $\text{FA}_{0.85}\text{Cs}_{0.15}\text{PbI}_3/\text{silica}$ interfaces with large areas, which should be a significant factor that contributes to stabilizing the $\text{FA}_{0.85}\text{Cs}_{0.15}\text{PbI}_3$ perovskite grains.

The device stability of the FAPI-T and FAPI films based PSCs are also compared. In the accelerated tests, 25 °C and 80% RH conditions are used. Figure S11 in the Supporting Information shows the monitored PCE evolution as a function of storage time of the PSC devices. Note that the PCE here is the stabilized PCE tested at $V = 0.91$ V. It can be seen that 80% of the initial PCE is retained for the FAPI-T film-based PSC after 24 h, while only 40% is retained for the FAPI film-based PSC. We have further tested the long-term stability of these PSCs in a relatively dry ambient condition (25 °C, 10% RH) and the results are shown in Figure 5A. The silica-free PSC device lost 60% of its initial PCE after ≈ 200 h storage. In contrast, the PCE of the silica-incorporated PSC only shows a very slight decay (3%) of its initial value after 168 h. Then, no obvious

performance decay is found in the continued test up to 1000 h. $J-V$ curves of the FAPI-T-based PSC before and after 1000 h are compared in Figure 5B, which shows only a slight reduction in FF that is responsible for the small PCE decrease. These results have confirmed the outstanding ambient-stability of PSCs based on the silica encapsulation method. Note that conventional TiO_2 and Spiro-OMeTAD charge transport layers are still used in our PSCs. In this context, we envision that by adopting the silica-encapsulated perovskite films in those emerging PSC architectures with alternative charge-transporting layers, such as BaSnO_3 and NiO_x ,^[41,42] we may achieve even more stable PSCs in the future.

The above results have confirmed that encapsulating FA-based perovskite grains with the optimal silica thin-layer has two major beneficial effects. First, silica passivates the defects/traps that can evolve during the solution processing. Especially, the incorporation of silica exhibits a unique merit in improving the film surface properties that can be key to the overall performance of perovskite solar cells. Second, silica fully encapsulates FA-based perovskite grains at the nanoscale, which has elegantly mitigated the widely concerned ambient-stability issue in FA-based perovskites. The physical isolation of individual perovskite grains and the reduction of chemical driving force for the undesirable perovskite-to-nonperovskite phase-transformation

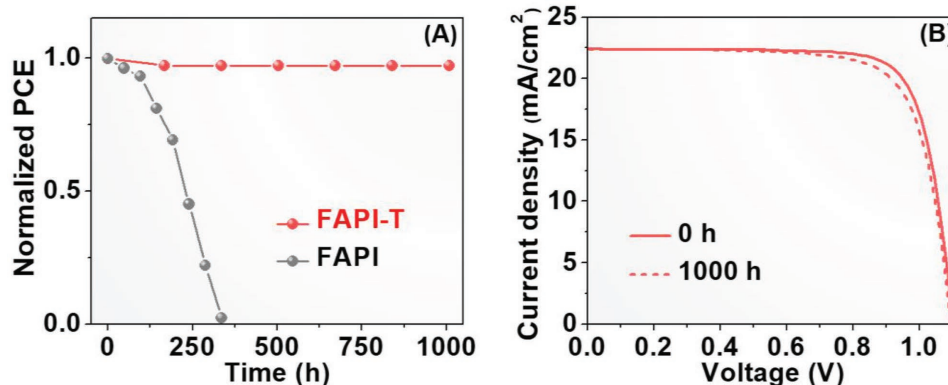


Figure 5. A) PCE evolution of the PSCs made using FAPI-T and FAPI film in the controlled ambient conditions (25 °C, 10% RH). B) J - V curves of the same FAPI-T-based PSC obtained before and after the 1000-h storage under controlled ambient conditions (25 °C, 10% RH).

are responsible for the significantly enhanced ambient stability. These combined effects simultaneously improve the efficiency and stability of FA-based PSCs.

In summary, we demonstrated here a new film structure for fabricating efficient stable FA-based PSCs, where the individual perovskite grains are fully encapsulated by in situ formed silica. This new concept is generic in nature for the application to PSCs made with various perovskite compositions. The success of this concept points out a new direction in engineering perovskite grains at the nanoscale within the polycrystalline perovskite films for the application to solar cells and other optoelectronics.

Experimental Section

Substrates and Raw Materials Preparation: FTO-coated glasses (Hartford Glass, USA) were etched with zinc powder (Sigma-Aldrich, USA) and hydrochloric acid (Sigma-Aldrich, USA) for the desired device pattern, followed by soaking in aqueous alkali solution (5% wt NaOH in ethanol) overnight. The patterned substrates are then washed with soap water, deionized water, and ethanol sequentially. Lead iodide (PbI_2) and $\text{HC}(\text{NH}_2)_2\text{I}$ (FAI) were purchased from Alfa Aesar, USA and DeySol, Australia, respectively. Cesium iodide (CsI), 2,2',7,7'-tetrakis-(*N,N*-di-4-methoxyphenylamino)-9,9'-spirobifluorene (Spiro-OMeTAD), bis(trifluoromethane) sulfonimide lithium salt (Li-TFSI) and TEOS, *N,N*-dimethylmethanamide (DMF), dimethylsulfoxide (DMSO), 4-tert-butylpyridine (TBP), acetonitrile (ACN), and chlorobenzene were purchased from Sigma-Aldrich, USA. All the chemicals were used as received.

Precursors and Films Preparation: FAPbI_3 solution was prepared by dissolving equimolar of PbI_2 and FAI in the mixed solvent of DMF and DMSO (7:3 v/v) at the concentration of 1 M. Separately, CsPbI_3 solution was prepared by dissolving equimolar of PbI_2 and CsI in the same DMF/DMSO mixed solvent at the concentration of 1 M. FAPI precursor solution was prepared by mixing FAPbI_3 and CsPbI_3 solutions at the volume ratio of 0.85:0.15. FAPI-T solutions were prepared by adding 30 μL TEOS and 6 μL H_2O into 1 ml $\text{FA}_{0.85}\text{Cs}_{0.15}\text{PbI}_3$ solution and shaking for 1 min. All solutions were prepared at room temperature and filtered with 0.22 μm polytetrafluoroethylene (PTFE) filters before use. Before the use, all solutions were aged for 30 min after the preparation. Perovskite films were deposited through a spin-coating process that involves three steps. The first step is 500 rpm for 5 s, the second step is 3000 rpm for 10 s, and the third step is 5000 rpm for 30 s. Toluene (1 mL) was dropped onto the centers of the spinning films 10 s before

the end. Subsequently, the films were annealed on a hotplate at 170 °C for 10 min.

Materials Characterization: Surface morphologies of films were observed by a SEM (LEO 1530VP, Carl Zeiss, Germany). XRD patterns were measured using an X-ray diffractometer (XRD; D8 Discover, Bruker, Germany) with $\text{Cu K}\alpha$ radiation. UV-vis absorption spectra were tested by a UV-vis spectrometer (UV-2600, Shimadzu Scientific, Japan). The film-stability tests were performed by storing the film samples in a climate chamber (MEMory CardXL, Memmert, Germany) with a constant relative humidity of 80% and temperature of 25 °C. Each time when the samples were taken out for a measurement, there occurs a variation of $\pm 5\%$ in the humidity in the chamber. Note that such film-stability tests are not "standard," and the results from which are not suitable for direct comparison with other reported stability results in the literature. High-resolution characterization was performed using a transmission electron microscope (TEM; 2100F, JEOL, Japan) operated at 200 kV accelerating voltage. Film samples for TEM studies were prepared by directly depositing the films on TEM grids (SPI Supplies, USA). The transit absorption (TA) measurements were conducted by using femtosecond monochromatic pump pulses and nanosecond broadband probe pulses (EOS, Ultrafast System, USA). The pump laser wavelength is 500 nm and the probe band spans from 400 nm to 800 nm. The steady-state PL spectra were measured at 797 nm upon excitation at 470 nm via a fluorescence spectrophotometer (FLS920, Edinburgh Instruments, England).

DFT Computations: First-principles calculations were performed using the projected augmented wave (PAW) plane-wave basis, implemented in the Vienna ab initio simulation package. An energy cutoff of 520 eV was employed and the atomic positions were optimized using the conjugate gradient scheme without any symmetric restrictions until the maximum force on each of them is less than 0.04 eV \AA^{-1} . The interface was modeled with Γ grid for the k-point sampling. The generalized gradient approximation exchange-correlation DFT functional Perdew-Burke-Ernzerhof with DFT-D3 which includes the dispersion interaction was employed for the geometrical optimization.

Device Fabrication and Testing: The compact TiO_2 layer was deposited on the patterned FTO-coated glasses by spray pyrolysis of 0.2 M titanium diisopropoxide bis(acetylacetonate) in 1-butanol at 450 °C. After further annealing at 450 °C for 1 h and cooling down to room temperature, TiO_2 -coated substrates were treated with UV-Ozone for 15 min. Perovskite films were deposited onto TiO_2 blocking layers using the procedure described above. Then, hole-transporting layers were deposited by spin-coating the Spiro-OMeTAD solution, which contains 80 mg Spiro-OMeTAD, 32 μL 4-TBP, 20 μL Li-TFSI stock solution (520 mg mL^{-1} in ACN), and 32 μL FK102 Co (III) TFSI salt stock solution (300 mg mL^{-1} in ACN). Finally, 80 nm of Au was evaporated onto the top of devices with a shadow mask. EQE spectra were recorded by a solar cell quantum efficiency measurement system (QEX10, PV Measurements, USA) at a

chopping frequency of 5 Hz in AC mode. Current density–voltage (J – V) curves were recorded by a SourceMeter (2400, Keithley, USA) under a simulated Air Mass (AM) 1.5G one-sun illumination (100 mW cm⁻², Oriol Sol3A Class AAA Solar Simulator, Newport Corporation, USA). The typical active area is 0.12 cm² defined using a nonreflective mask. The steady-state current/power outputs were monitored with a VersaSTAT MC potentiostat (Princeton Applied Research, USA). Device stability is evaluated by monitoring the steady-state PCE at $V = 0.91$ V, upon storage of the PSC devices in a controlled humidity and constant 25 °C in a climate chamber (MEMory CardXL, Memmert, Germany).

Supporting Information

Supporting Information is available from the Wiley Online Library or from the author.

Acknowledgements

T.L., D.L., W.Y., R.Z., and Q.G. acknowledge the funding from 973 Program of China (2015CB932203), National Natural Science Foundation of China (61722501, 61377025, 91433203, and 91733301) and Young 1000 Talents Global Recruitment Program of China. T.L., Y.Z., L.Z., and N.P.P. thank the funding from National Science Foundation (OIA-1538893) and the Office of Naval Research (N00014-17-1-2232) for the research funding. M.-G.J. and X.C.Z. thank National Science Foundation (OIA-1538893). The work at the National Renewable Energy Laboratory was supported by the U.S. Department of Energy under Contract No. DE-AC36-08-GO28308 with Alliance for Sustainable Energy, Limited Liability Company (LLC), the Manager and Operator of the National Renewable Energy Laboratory. M.Y., Z.L., D.H.K., and K.Z. acknowledge the hybrid perovskite solar cell program funded by the U.S. Department of Energy, Office of Energy Efficiency and Renewable Energy, Solar Energy Technologies Office. Y.Y. and M.C.B. acknowledge the Division of Chemical Sciences, Geosciences, and Biosciences, Office of Basic Energy Sciences, Office of Science within the U.S. Department of Energy.

Conflict of Interest

The authors declare no conflict of interest.

Keywords

charge transport, encapsulate, perovskite, silica, stability

Received: January 22, 2018

Revised: March 26, 2018

Published online:

- [1] S. D. Stranks, G. E. Eperon, G. Grancini, C. Menelaou, M. J. P. Alcocer, T. Leijtens, L. M. Herz, A. Petrozza, H. J. Snaith, *Science* **2013**, 342, 341.
- [2] G. Xing, N. Mathews, S. Sun, S. S. Lim, Y. M. Lam, M. Graetzel, S. Mhaisalkar, T. C. Sum, *Science* **2013**, 342, 344.
- [3] M. A. Green, A. Ho-Baillie, H. J. Snaith, *Nat. Photonics* **2014**, 8, 506.
- [4] A. Kojima, K. Teshima, Y. Shirai, T. Miyasaka, *J. Am. Chem. Soc.* **2009**, 131, 6050.
- [5] H.-S. Kim, C. R. Lee, J. H. Im, K. B. Lee, T. Moehl, A. Marchioro, S. J. Moon, R. Humphrey Baker, J. H. Yum, J. E. Moser, M. Graetzel, N. G. Park, *Sci. Rep.* **2012**, 2, 591.
- [6] J. Burschka, N. Pellet, S. J. Moon, R. Humphrey-Baker, P. Gao, M. K. Nazeeruddin, M. Gratzel, *Nature* **2013**, 499, 316.
- [7] M. Liu, M. B. Johnston, H. J. Snaith, *Nature* **2013**, 501, 395.
- [8] T. Liu, Q. Hu, J. Wu, K. Chen, L. Zhao, F. Liu, C. Wang, H. Lu, S. Jia, T. Russell, R. Zhu, Q. Gong, *Adv. Energy Mater.* **2016**, 6, 1501890.
- [9] N. J. Jeon, J. H. Noh, Y. C. Kim, W. S. Yang, S. Ryu, S. I. Seok, *Nat. Mater.* **2014**, 13, 897.
- [10] N. J. Jeon, J. H. Noh, W. S. Yang, Y. C. Kim, S. Ryu, J. Seo, S. I. Seok, *Nature* **2015**, 517, 476.
- [11] J. B. You, Y. M. Yang, Z. R. Hong, T. B. Song, L. Meng, Y. S. Liu, C. Y. Jiang, H. P. Zhou, W. H. Chang, G. Li, Y. Yang, *Appl. Phys. Lett.* **2014**, 105, 183902.
- [12] H. Zhou, Q. Chen, G. Li, S. Luo, T.-B. Song, H.-S. Duan, Z. Hong, J. You, Y. Liu, Y. Yang, *Science* **2014**, 345, 542.
- [13] W. S. Yang, J. H. Noh, N. J. Jeon, Y. C. Kim, S. Ryu, J. Seo, S. I. Seok, *Science* **2015**, 348, 1234.
- [14] M. Saliba, T. Matsui, J. Y. Seo, K. Domanski, J. P. Correa Baena, M. K. Nazeeruddin, S. M. Zakeeruddin, W. Tress, A. Abate, A. Hagfeldt, M. Gratzel, *Energy Environ. Sci.* **2016**, 9, 1989.
- [15] W. S. Yang, B. W. Park, E. H. Jung, N. J. Jeon, Y. C. Kim, D. U. Lee, S. S. Shin, J. Seo, E. K. Kim, J. H. Noh, S. I. Seok, *Science* **2017**, 356, 1376.
- [16] D. Luo, L. Zhao, J. Wu, Q. Hu, Y. Zhang, Z. Xu, Y. Liu, T. Liu, K. Chen, W. Yang, W. Zhang, R. Zhu, Q. Gong, *Adv. Mater.* **2017**, 29, 1604758.
- [17] Research Cell Efficiency Records. NREL., <https://www.nrel.gov/pv/assets/images/efficiency-chart.png>, (accessed: March 2018).
- [18] G. E. Eperon, S. D. Stranks, C. Menelaou, M. B. Johnston, L. M. Herz, H. J. Snaith, *Energy Environ. Sci.* **2014**, 7, 982.
- [19] a) S. Pang, H. Hu, J. Zhang, S. Lv, Y. Yu, F. Wei, T. Qin, H. Xu, Z. Liu, G. Cui, *Chem. Mater.* **2014**, 26, 1485; b) S. K. Yadavalli, Y. Zhou, N. P. Padture, *ACS Energy Lett.* **2018**, 3, 63.
- [20] A. Binek, F. C. Hanusch, P. Docampo, T. Bein, *J. Phys. Chem. Lett.* **2015**, 6, 1249.
- [21] T. M. Koh, K. Fu, Y. Fang, S. Chen, T. C. Sum, N. Mathews, S. G. Mhaisalkar, P. P. Boix, T. Baikie, *J. Phys. Chem. C* **2014**, 118, 16458.
- [22] C. C. Stoumpos, C. D. Malliakas, M. G. Kanatzidis, *Inorg. Chem.* **2013**, 52, 9019.
- [23] T. Liu, Y. Zong, Y. Zhou, M. Yang, Z. Li, O. S. Game, K. Zhu, R. Zhu, Q. Gong, N. P. Padture, *Chem. Mater.* **2017**, 29, 3246.
- [24] Z. Li, M. Yang, J. S. Park, S. H. Wei, J. J. Berry, K. Zhu, *Chem. Mater.* **2016**, 28, 284.
- [25] J. W. Lee, D. H. Kim, H. S. Kim, S. W. Seo, S. M. Cho, N. G. Park, *Adv. Energy Mater.* **2015**, 5, 1501310.
- [26] M. Saliba, T. Matsui, K. Domanski, J. Y. Seo, A. Ummadisingu, S. M. Zakeeruddin, J. P. Correa Baena, W. R. Tress, A. Abate, A. Hagfeldt, M. Gratzel, *Science* **2016**, 354, 206.
- [27] Z. Wang, Q. Lin, F. P. Chmiel, N. Sakai, L. M. Herz, H. J. Snaith, *Nat. Energy* **2017**, 2, 17135.
- [28] L. N. Quan, M. Yuan, R. Comin, O. Voznyy, E. M. Beauregard, S. Hoogland, A. Buin, A. R. Kirmani, K. Zhao, A. Amassian, D. H. Kim, E. H. Sargent, *J. Am. Chem. Soc.* **2016**, 138, 2649.
- [29] N. Li, Z. Zhu, C. C. Chueh, H. Liu, B. Peng, A. Petrone, X. Li, L. Wang, K. Y. Jen Alex, *Adv. Energy Mater.* **2016**, 7, 1601307.
- [30] a) A. M. Buckley, M. Greenblatt, *J. Chem. Educ.* **1994**, 71, 599; b) B. A. de Carvalho, S. Kavadiya, S. Wang, D. M. Niedzwiedzki, P. Biswas, *IEEE J. Photovolt.* **2017**, 7, 532.
- [31] S. Huang, Z. Li, L. Kong, N. Zhu, A. Shan, L. Li, *J. Am. Chem. Soc.* **2016**, 138, 5749.
- [32] a) Y. Zhou, A. L. Vasiliev, W. Wu, M. Yang, S. Pang, K. Zhu, N. P. Padture, *J. Phys. Chem. Lett.* **2015**, 6, 2292; b) Y. Zong, Y. Zhou, Y. Zhang, Z. Li, L. Zhang, M.-G. Ju, M. Chen, S. Pang,

- X. C. Zeng, N. P. Padture, *Chem.* **2018**, <https://doi.org/10.1016/j.chempr.2018.03.005>.
- [33] M. U. Rothmann, W. Li, Y. Zhu, U. Bach, L. Spiccia, J. Etheridge, Y. B. Cheng, *Nat. Commun.* **2017**, *8*, 14547.
- [34] F. Ji, S. Pang, L. Zhang, Y. Zong, G. Cui, N. P. Padture, Y. Zhou, *ACS Energy Lett.* **2017**, *2*, 2727.
- [35] Y. Yang, M. Yang, D. T. Moore, Y. Yan, E. M. Miller, K. Zhu, M. C. Beard, *Nat. Energy* **2017**, *2*, 16207.
- [36] Y. Yang, Y. Yan, M. Yang, S. Choi, K. Zhu, J. M. Luther, M. C. Beard, *Nat. Commun.* **2015**, *6*, 7961.
- [37] M. Yang, Y. Zeng, Z. Li, D. H. Kim, C. S. Jiang, J. van de Lagemaat, K. Zhu, *Phys. Chem. Chem. Phys.* **2017**, *19*, 5043.
- [38] J. Huang, S. Tan, P. D. Lund, H. Zhou, *Energy Environ. Sci.* **2017**, *10*, 2284.
- [39] Y. Zhou, J. Kwun, H. F. Garces, S. Pang, N. P. Padture, *Chem. Commun.* **2016**, *52*, 7273.
- [40] M. Saliba, T. Matsui, K. Domanski, J. Y. Seo, A. Ummadisingu, S. M. Zakeeruddin, J.-P. Correa Baena, W. Tress, A. Abate, A. Hagfeldt, M. Graetzel, *Science* **2016**, *354*, 206.
- [41] S. S. Shin, E. J. Yeom, W. S. Yang, S. Hur, M. G. Kim, J. Im, J. Seo, J. H. Noh, S. I. Seok, *Science* **2017**, *356*, 167.
- [42] X. Zhao, H. S. Kim, J. Y. Seo, N. G. Park, *ACS Appl. Mater. Interfaces* **2017**, *9*, 7148.